

Successful νp -process in neutrino-driven outflows in core-collapse supernovae

Alexander Friedland,^{1,*} Payel Mukhopadhyay,^{1,2,3,†} and Amol V. Patwardhan^{1,4,‡}

¹SLAC National Accelerator Laboratory, Menlo Park, CA 94025, USA

²Physics Department, Stanford University, Stanford, CA 94305, USA

³Department of Physics, University of California, Berkeley, Berkeley, CA 94720, USA

⁴School of Physics and Astronomy, University of Minnesota, Minneapolis, MN 55455, USA

(Dated: December 5, 2023)

The origin of the solar system abundances of several proton-rich isotopes, especially $^{92,94}\text{Mo}$ and $^{96,98}\text{Ru}$, has been an enduring mystery in nuclear astrophysics. An attractive proposal to solve this problem is the νp -process, which can operate in neutrino-driven outflows in a core-collapse supernova after the shock is launched. Years of detailed studies, however, have cast doubt over the ability of this process to generate sufficiently high absolute and relative amounts of various p -nuclei. The νp -process is also thought to be excluded by arguments based on the long-lived radionuclide ^{92}Nb . Here, we present explicit calculations, in which both the abundance ratios and the absolute yields of the p -nuclei up to $A \lesssim 105$ are successfully reproduced, even when using the modern (medium enhanced) triple- α reaction rates. The process is also shown to produce the necessary amounts of ^{92}Nb . The models are characterized by subsonic outflows and by the proton-neutron star masses in the $\gtrsim 1.7M_{\odot}$ range. This suggests that the Mo and Ru p -nuclides observed in the Solar System were made in CCSN explosions characterized by an extended accretion stage.

Most of the trans-iron elements in nature are synthesized by slow or rapid neutron capture, the s - and r -processes [1–3]. These processes, however, bypass 35 naturally occurring proton-rich isotopes, the origin of which has been a classic problem in nuclear astrophysics [1, 4, 5]. Some of the p -nuclides can be created by the photodisintegration of preexisting s -process isotopes in exploding stars (the γ -process) [6–8]. Yet, it was shown that the solar s -process isotope abundances are insufficient [5, 6, 9, 10] to explain all p -nuclei observations. Particularly challenging [5, 9] are $^{92,94}\text{Mo}$ and $^{96,98}\text{Ru}$, whose abundances are comparable to those of the corresponding s -process isotopes [6, 11]. Even positing large s -process enrichment before a Type-Ia explosion, the observed abundances of ^{94}Mo cannot be obtained [12, 13].

One is thus led to nucleosynthetic paths involving proton capture. This requires not only a proton-rich medium, but also a specific temperature window, $1.5\text{ GK} \lesssim T \lesssim 3\text{ GK}$ [14]. In this window, the temperature is high enough to overcome Coulomb repulsion, but not so high as to bring heavy nuclei into quasi-equilibrium with the iron group [15]. The classical rp -process, however, encounters a difficulty: in typical astrophysical settings, the material spends less than a second in this temperature range, while the reaction chain includes several longer-lived isotopes, which create *waiting points* that prevent the synthesis of heavier p -isotopes [16].

An elegant proposal that evades this difficulty is the νp -process [10, 17, 18]. It operates in the innermost ejecta of a core-collapse supernova (CCSN), in an outflow of high-entropy matter from the surface of the pro-

ton-neutron star (PNS) that forms after the explosion is launched [10, 14, 17–31]. A physically plausible choice of neutrino and antineutrino spectra makes the outflow proton-rich (electron fraction $Y_e \sim 0.6$). As the outflow material expands and cools, some of the nucleons assemble into heavy elements. The large neutrino flux not only powers the outflow, but also creates a subdominant neutron population in the proton-rich medium. These neutrons are promptly captured on the proton-rich seeds, in reactions that bypass the beta-decay waiting points.

Several quantitative studies, however, have identified a number of difficulties in explaining the observed p -nuclide abundances with the νp -process [5, 28–31]. Various calculations in these papers: (i) did not reproduce the observed solar system abundance ratios of $^{92}\text{Mo}/^{94}\text{Mo}$ [28–30] and $^{96}\text{Ru}/^{98}\text{Ru}$ isotopes [30]; (ii) significantly underproduced the absolute amounts of $^{92,94}\text{Mo}$ and $^{96,98}\text{Ru}$ compared to the fiducial astrophysical model [14, 32], especially when incorporating modern, medium-enhanced triple- α reaction rates [31, 33]; (iii) significantly overproduced the lighter p -nuclides, ^{74}Se , ^{78}Kr , ^{84}Sr , compared to $^{92,94}\text{Mo}$ and $^{96,98}\text{Ru}$ [30]; (iv) did not account for [5] the presence of the ^{92}Nb isotope in the early solar system [34, 35]; and, finally, (v) observed that, under certain conditions, the final isotopic composition of the outflow could be driven to the neutron-rich side [19].

In view of such a long list of difficulties, it appeared unlikely that all these conditions could be satisfied within a consistent outflow model, without ad hoc adjustment of parameters to unphysical values. As a result, the current understanding of the origin of the p -isotopes is considered to be as uncertain as ever [5, 31]. Yet, as shown below, a subclass of CCSN explosions naturally hosts conditions in which all of these difficulties are resolved.

* alexfr@slac.stanford.edu

† pmukho@berkeley.edu

‡ apatward@umn.edu

I. RESULTS

A. Snapshots of subsonic and supersonic outflows

The νp -process involves out-of-equilibrium dynamics, which makes its yields very sensitive to the outflow hydrodynamics [14]. To test the viability of the νp -mechanism, one needs to scan the range of possible outflow conditions. This cannot be achieved by computing yields for a specific high-fidelity numerical simulation: a negative result would not exclude the mechanism for all physically plausible explosion scenarios. Accordingly, we consider a suite of physical 1D models which span the range of conditions (the same argument is made in, e.g., [30]). If the viability is established in any of the regimes, it can be targeted for follow-up with detailed multi-D simulations.

The key consideration that dictates which conditions should be scanned is the *near-criticality* of the neutrino-driven outflows in a CCSN: they are close to the transition between subsonic and supersonic regimes [36]. A fixed supersonic ansatz with variable entropy and electron fraction misses the subsonic regime altogether [31]. In our study, we vary *the physical conditions* that determine the nature of the outflow: the properties of the PNS, the progenitor star mass, and the neutrino fluxes (see Methods for details). We find that subsonic outflows produce much greater yields of the desired p -nuclides than the supersonic ones.

This is shown in Fig. 1, where instantaneous yields are compared for our $9.5 M_{\odot}$ and $13 M_{\odot}$ progenitor models. In the first case, the outflow accelerates to supersonic speeds and then runs into the surrounding slower moving material forming a termination shock. This is the traditional neutrino-driven “wind” regime [37–39]. In the second case, the greater mass swept up by the front shock creates a sufficient surrounding pressure to keep the outflow speed subsonic. In both cases, the outflows are proton-rich, with $Y_e \sim 0.6$ at small radii, and the PNS radius is 19 km, typical for 1–2 s after the shock launch. Notably, the PNS mass in the $13 M_{\odot}$ progenitor case is $1.8 M_{\odot}$. This is necessary to obtain total entropy per baryon $S_{\text{tot}} \simeq 90$ (or *radiation* entropy per baryon $S \simeq 74$), as discussed below. The details of both models are supplied in the Methods section.

For comparison, a calculation from Ref. [31] with a parametrized wind outflow profile with $S_{\text{tot}} = 80$ is also shown. It is seen that the results in that case are close to our supersonic model. The main conclusion is that the yields of $^{92,94}\text{Mo}$ and $^{96,98}\text{Ru}$ in the model with a subsonic outflow—the regime previously overlooked in the context of the νp -process—are 1–2 orders of magnitude higher than with the supersonic wind.

We also examine the amounts of ^{92}Nb synthesized in these calculations. Surprisingly, in the subsonic case it is produced in the necessary amounts to explain the solar system observations, while the standard lore says that this nuclide should not be made at all in the νp -process [5]. We discuss this further in Secs. IB and IC.

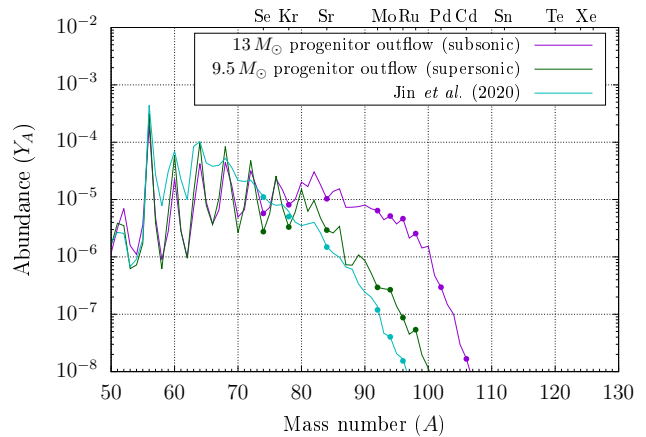


FIG. 1. Time snapshots of nucleosynthesis yields in our models with a subsonic outflow ($13 M_{\odot}$ progenitor) and a supersonic outflow ($9.5 M_{\odot}$ progenitor). Also reproduced is a calculation from Ref. [31] with a parametrized supersonic outflow profile with entropy $S_{\text{tot}} = 80$. Nominal in-medium enhanced triple- α rates from Ref. [31] are assumed throughout. The p -nuclei yields for $A > 90$ are greater by 1–2 orders of magnitude in the subsonic regime compared to the supersonic cases.

B. Stages of the νp -process

To gain insight into these numerical results, we analyze the physics of the νp -process. Fig. 2 shows the snapshots in the neutron-proton plane from our simulation of the $13 M_{\odot}$ progenitor model. The four stages are described in the caption. Several conditions must be matched between these stages. Let us investigate these in turn.

First, consider stages I and II. Efficiency of neutron production during stage II controls how high in atomic number the nucleosynthesis chain progresses. To produce sufficient amounts of $^{92,94}\text{Mo}$ and $^{96,98}\text{Ru}$ requires about ten neutrons per iron-group seed [14]. Supersonic outflows tend to overproduce seeds compared to neutrons. In subsonic outflows, however, stage II occurs *closer* to the PNS surface, where the material is subjected to a greater flux of neutrinos. As a result, up to three times as many neutrons are created as in the supersonic case, a fact not appreciated before.

The factor counteracting this is the in-medium enhancement of the triple- α reaction [31, 33]. In proton-rich conditions, only a small fraction of the outflow, about 3–5% by mass, progresses to the iron group nuclei, while most nucleons remain in the form of α -particles (about 80% by mass). The bottleneck occurs [14] at the formation of ^{12}C : $\alpha + \alpha + \alpha \rightleftharpoons {}^8\text{Be}^* + \alpha \rightleftharpoons {}^{12}\text{C}^*$ create an excited state of $^{12}\text{C}^*$ —the Hoyle state—that in most cases dissociates back into alpha particles. The formation of the ground state of ^{12}C occurs by radiative decay of the Hoyle state and, in dense plasma, also by collisions [33] with protons and neutrons in the medium.

We find, however, that the neutron production rate during the second stage is so large in the subsonic case,

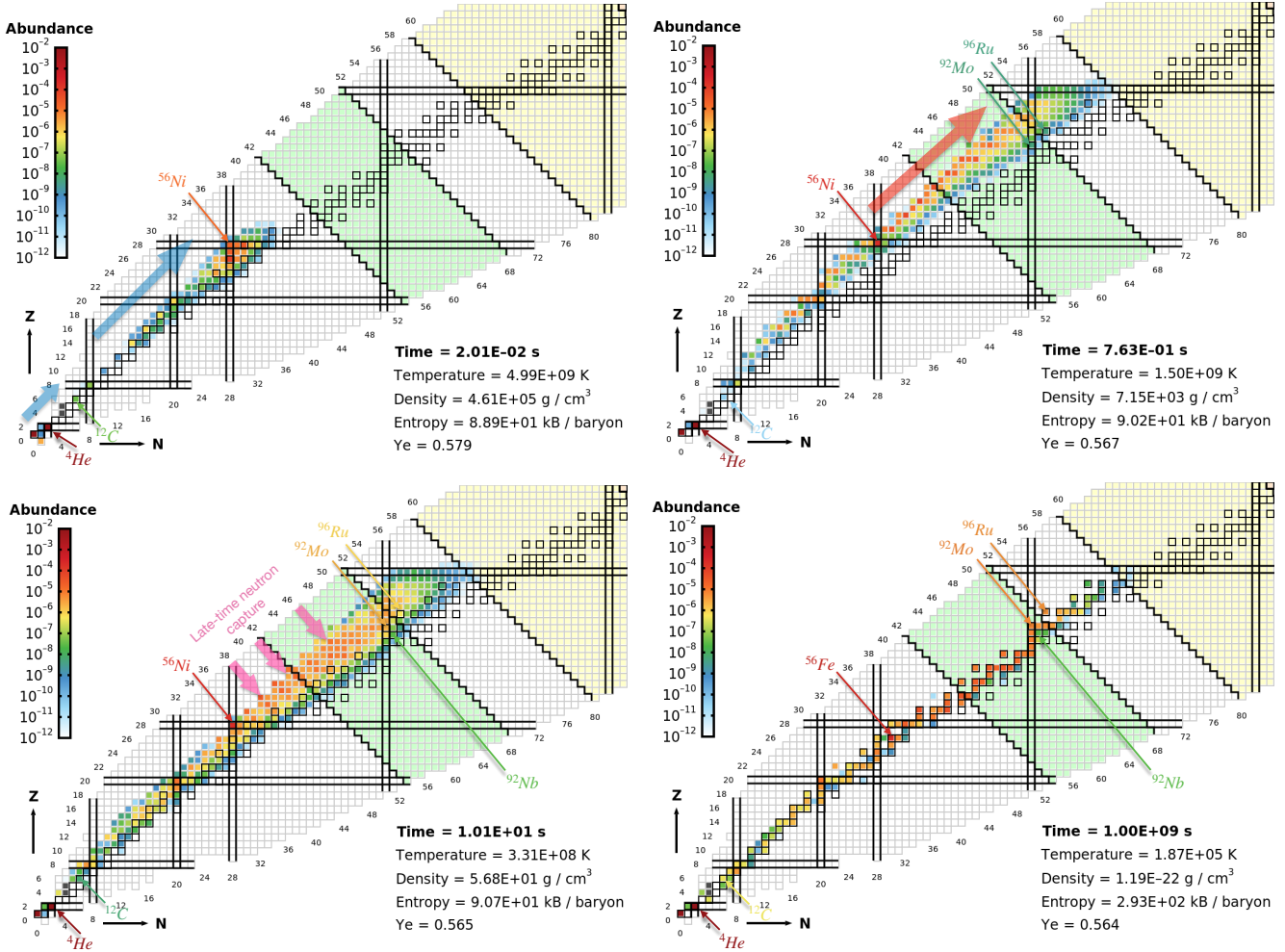


FIG. 2. Stages of the νp -process in a proton-rich outflow ($13 M_{\odot}$ progenitor model). *Top left* (stage I): while $3 \text{ GK} \lesssim T \lesssim 6 \text{ GK}$, the outflow is made mostly of α -particles and excess protons; the triple- α bottleneck ensures that only a small fraction of the α -particles assemble into iron-group seeds. *Top right* (stage II): in the window $1.5 \text{ GK} \lesssim T \lesssim 3 \text{ GK}$, proton capture, assisted by the capture of neutrons made in neutrino interactions, drives the formation of proton-rich isotopes in the mass range $64 \lesssim A \lesssim 105$. *Bottom left* (stage III): below $T \sim 1.5 \text{ GK}$, proton capture becomes suppressed by the Coulomb barrier; neutrino interactions on free protons, however, continue neutron production; the resulting late-time (n, γ) and (n, p) reactions bring the composition closer to the valley of stability. *Bottom right* (stage IV): by $t \sim 10^9 \text{ s}$, late-time β -decays complete the formation of (meta)stable isotopes. Notice the presence of shielded isotopes, including ^{92}Nb , that could not be created by the β -decays only.

that even with the in-medium enhancement of the triple- α rate the neutron-to-seed ratio is still optimal, so long as radiation entropy per baryon is $S \gtrsim 65$ in the outflow (which is also used in [31]). In our self-consistent model, S is not an independent parameter, but is set by the physical properties of the PNS. Specifically, S is related to the gravitational potential at the PNS surface [38], which, given the physical constraints on the PNS radius at this stage of the explosion, translates into a lower bound on the PNS mass, $M_{\text{PNS}} \gtrsim 1.7 M_{\odot}$. This is one of the key findings of our study and we will elaborate on it below.

We now turn to neutron production during stage III. We checked that, in our subsonic outflows, these neutrons do not drive the composition beyond the valley of

stability to the neutron-rich side (cf. [19]). This finding is nontrivial as there are no more independent physical parameters left to be adjusted in our model. Even more remarkably, the number of the late-time neutrons found in our calculation—3–6 per seed—turns out to be optimal for solving the ^{92}Nb origin problem. The standard lore says that isotopes such as ^{92}Nb or ^{98}Tc , which are shielded from β -decays by stable isotopes, cannot be produced in the νp -process at all. This assertion, which originates from the studies of the classical rp -process [42] and is reinforced by an unfortunate severe bug in the `ReacLib` library (see *Methods*), turns out to be erroneous when applied to the νp -process. Both ^{92}Nb and ^{98}Tc are produced by neutron capture during stage III.

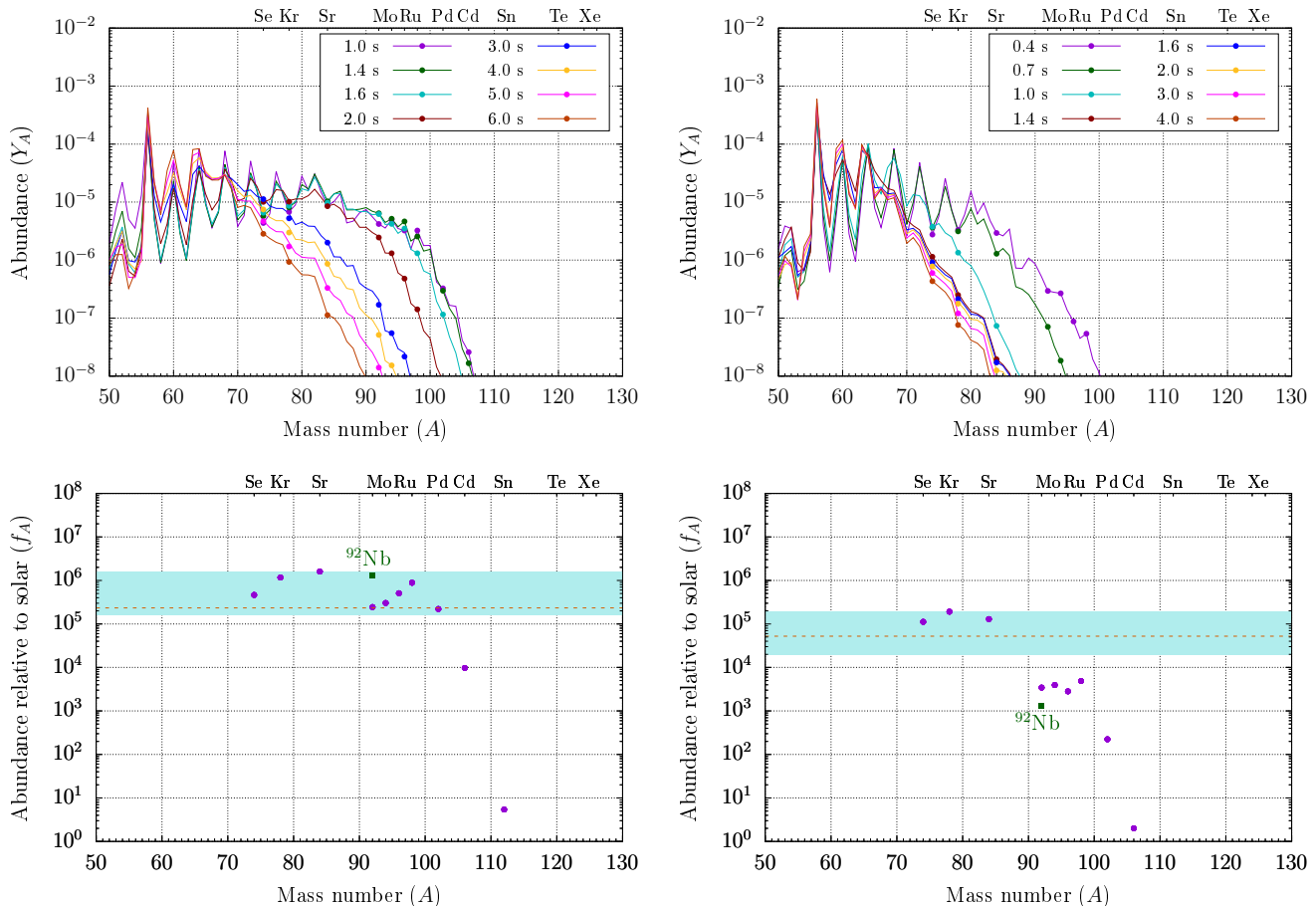


FIG. 3. *Top panels:* Snapshots of nucleosynthetic yields from the explosions of $13 M_{\odot}$ (left) and $9.5 M_{\odot}$ (right) progenitors, labeled by the particle launch times. *Bottom panels:* Integrated production factors (abundances relative to solar) of the p -nuclides of interest. The orange dashed line represents the minimum needed to explain the absolute abundances of these isotopes in the solar system [14, 32]. The colored band denotes the range of production factors between f_{\max} and $f_{\max}/10$, where f_{\max} is the highest production factor among all the p -nuclides. The subsonic outflow in the $13 M_{\odot}$ model produces all the p -nuclides up to ^{102}Pd within the colored band and above the dashed line. It also produces the desired amount of ^{92}Nb , whose integrated production factor here is normalized to 3×10^{-3} of the solar ^{92}Mo abundance, as suggested by studies of meteorites, cf. [5, 34, 40, 41]. The supersonic outflow in the $9.5 M_{\odot}$ model significantly underproduces p -nuclides above ^{84}Sr .

C. Integrated yields

For quantitative comparisons with the solar system abundances, one should use time-integrated, rather than instantaneous, yields. We compute yields across a sequence of outflow snapshots, corresponding to the trajectories of particles launched from the PNS surface at various times t_{ps} after the shock revival (hereafter “post-shock time”). These yields are integrated, weighted by the corresponding mass loss rates $\dot{M}(t)$, as detailed in Sec. IID. The results are shown in Fig. 3. The left panels depict our calculations for the $13 M_{\odot}$ progenitor model, where the outflow remains subsonic for the duration of the explosion. The right panels show the corresponding results for the $9.5 M_{\odot}$ progenitor model, where the outflow stays supersonic. In both cases, most of the p -nuclei with $A > 80$ are produced in a narrow time window.

This high-yield time window (HYTW) corresponds to the stage of the explosion when the material surrounding the hot bubble has temperature in the $1.5 \text{ GK} \lesssim T \lesssim 3 \text{ GK}$ range. The outflow upon deceleration reaches that temperature band and lingers in it for half a second or longer, allowing sufficient time for proton and neutron capture to drive p -isotope production [14]. In addition to the time spent in this temperature range, the *distance* to the PNS is another key factor. This distance is smaller in the subsonic case, allowing for sufficient neutron production to make the p -isotopes up to ^{102}Pd .

The HYTW onset changes with progenitor mass—a heavier progenitor experiences it later than a lighter one, as the swept-up mass needs to be further diluted in the first case. However, the existence of the HYTW is always guaranteed. Thus, the νp mechanism does not require progenitor mass fine-tuning—it is efficient in all suffi-

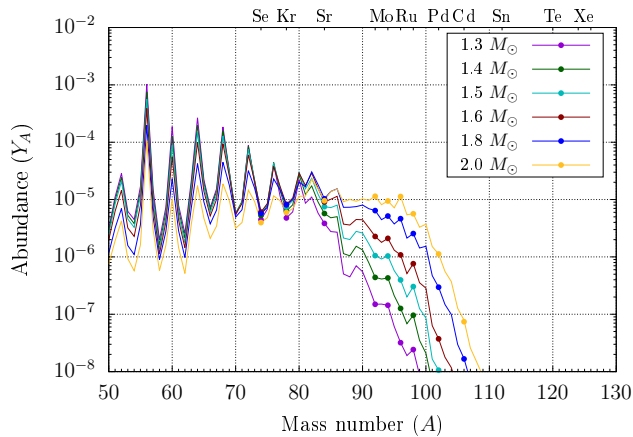


FIG. 4. νp -process yields for different proton-neutron star masses. The radius of the PNS is kept fixed at 19 km. Clearly, the νp -process yields improve with higher masses. Explosions with $M_{\text{PNS}} \gtrsim 1.7 M_{\odot}$ are ideal sites for the νp -process.

ciently massive progenitors in which the outflows are subsonic. Another important point is that the HYTW occurs within the first 1–2 s after the explosion is launched. At this time, the neutrino fluxes are still high and so is the amount of mass ejected. This makes it possible to generate sufficiently large absolute p -nuclide yields.

The bottom panels show the integrated yields, divided by the corresponding solar system abundances. The orange dashed line indicates the desired absolute amounts of each element [14, 32], while the shaded band shows the range of production factors (see Sec. IID) between f_{max} and $f_{\text{max}}/10$, where f_{max} is the maximum production factor among the p -nuclides. Isotopes falling in this band are co-produced in sufficient quantities relative to the isotope with the highest production factor [14, 30]. We see that the subsonic outflow of the $13 M_{\odot}$ progenitor model produces the correct amounts of all p -isotopes up to ^{102}Pd . Details of this analysis are given in Sec. IID.

Also shown in Fig. 3 is the production fraction of ^{92}Nb , normalized to the observations of ^{92}Mo , specifically to 3×10^{-3} times the solar ^{92}Mo abundance. This amount is sufficient to reconcile the solar system observations of ^{92}Zr , into which this unstable nuclide eventually decays [5, 34, 40, 41]. We can also make predictions for other shielded isotopes that are produced by late-time neutrons during stage III of the νp -process, such as ^{98}Tc , for which we predict $\sim 10^{-4}$ of the ^{98}Ru abundance. This is consistent with the available upper limit on this nuclide in the solar system [42], given its 6.1 Myr half-life.

D. Proton-neutron star properties

As already mentioned, the model with the successful νp process has the PNS mass of $1.8 M_{\odot}$. The physics underlying this choice is as follows. As the outflow expands,

seed production is triggered when it reaches a certain temperature, see Fig. 5. The efficiency of seed production is controlled by the matter density at that temperature, since the triple- α reaction rates are strongly density dependent. The relationship between density and temperature is expressed by the entropy-per-baryon ratio, S , which, in turn, is related to the gravitational potential near the PNS surface [38]. Thus, seed production depends on the ratio of the PNS parameters, $M_{\text{PNS}}/R_{\text{PNS}}$. Next, we need to consider the physical range of R_{PNS} . Most studies of the nuclear equation of state focus on the radius of a cold neutron star, which is typically in the range of 10–12 km. However, 1–2 s after the explosion is launched, the radius is larger, because the PNS still has a significant amount of trapped thermal energy and lepton number. Modern simulations report values in the range of 17–22 km [43–47]. Given this, to obtain the required value of S , the PNS mass has to be in the range $M_{\text{PNS}} \gtrsim 1.7 M_{\odot}$. This leads to not only the required absolute amounts of p -nuclides up to ^{102}Pd , but also the desired pattern of relative abundance ratios of $^{92,94}\text{Mo}$ and $^{96,98}\text{Ru}$. Instantaneous p -isotope yields for different PNS masses are shown in Fig. 4.

Our findings align nontrivially with modern simulations. The PNS mass is controlled by the amount of matter accreted onto the PNS post collapse. For light progenitors with masses of 9–10 M_{\odot} the explosion is achieved quickly and the resulting baryonic PNS mass is close to the Chandrasekhar value. For more massive progenitors, however, modern multi-dimensional simulations find that extended accretion is not only possible, but a common feature. For progenitors of 13–20 M_{\odot} , one finds PNS masses in the range 1.6–2.0 M_{\odot} [48].

E. Discussion

We have used a suite of one-dimensional semi-analytical models to survey the parameter space of the νp -process in CCSN. We uncovered a regime in which the conditions reproduce the solar system observations of p -nuclei up to ^{102}Pd , including the famous p -isotopes of Mo and Ru, and avoid all the objections raised in the literature. Several pieces fall into place in a nontrivial way. First, the desired abundance pattern is achieved for all parameters in their physically plausible ranges. Second, for sufficiently heavy progenitors, modern simulations find that the neutrino driven outflows are subsonic and the PNS is heavy due to an extended accretion stage. Third, late-time neutrons not only do not drive the composition to the neutron-rich side, but also produce the shielded ^{92}Nb in the correct abundance. All these results motivate and guide future investigations. It is desirable to assess the impact of different nuclear equations of state and of neutrino flavor transformations, including collective oscillations that may occur above the PNS surface. Above all, the regime found here deserves further investigation with modern multi-dimensional simulations.

II. METHODS

A. Outflow calculations

Each iteration of the nucleosynthesis calculation requires modeling matter trajectories through the stages depicted in Fig. 2. The matter starts out close to the PNS surface where nuclear statistical equilibrium prevails and is followed to a large radius until neutron capture ceases. This covers stages I through III in Fig. 2; the last stage involves only beta-decays, which does not require detailed trajectory modeling. The duration of stages I through III is comparable to the timescales on which the neutrino luminosities decay and the matter profile changes in the developing explosion. Therefore, the nucleosynthesis trajectories are not instantaneous snapshots of the matter profile. Yet, the physics of the problem affords an important simplification: the outflow can be divided into two segments. The first segment describes the acceleration of the material by neutrino heating near the PNS surface and its deceleration by the surrounding slowly expanding material. The second one involves the subsequent evolution upon joining the homologous expansion of the

material behind the front shock, following $v \sim \text{const}$ (cf. [14, 43]). The first segment is quick enough ($\lesssim 1$ s) to treat the outer boundary condition and the neutrino fluxes as approximately constant in time. The second one has time-varying ρ and T dictated by the expansion of the front shock, as well as neutrino luminosities variable on the PNS cooling timescale. This framework allows us to explore the yields as a function of physical conditions while avoiding using full SN simulations.

The first segment has been modeled numerically, by solving a set of steady-state, spherically symmetric equations. Our approach is based on the classical treatment of neutrino-driven outflows [37, 38], but with three important differences. First, we take into account general relativistic corrections [49]. Second, we incorporate the change in the effective number of relativistic degrees of freedom g_* , which occurs as the outflow cools through the temperature of e^+e^- annihilation between the PNS surface and the outer edges of the hot bubble [36]. Last, we consistently treat the far boundary condition, using the methodology described in [36], which treats subsonic and supersonic regimes, and the transition between the two, in a unified fashion. With this, and using the Schwarzschild background, we have [49]

$$\left(\frac{v}{1-v^2}\right) \left(1 - \frac{v_s^2}{v^2}\right) \frac{dv}{dr} = \frac{2v_s^2}{r} - \frac{GM}{r^2} \frac{(1-v_s^2)}{\left(1 - \frac{2GM}{r}\right)} - \beta \frac{\dot{q}}{vy(1+3v_s^2)}, \quad (1)$$

$$\frac{\dot{q}}{1+3v_s^2} = vy \frac{d}{dr} \left[\ln(1+3v_s^2) - \frac{1}{2} \ln(1-v^2) + \frac{1}{2} \ln\left(1 - \frac{2GM}{r}\right) \right], \quad (2)$$

$$vy \frac{dS}{dr} = \frac{\dot{q}m_N}{T}. \quad (3)$$

Here v is the coordinate velocity of the fluid element, v_s is the sound speed, S is radiation entropy per baryon and $y = \sqrt{(1-2GM/r)/(1-v^2)}$. Natural units are as-

sumed, so that the speed of light $c = 1$. Furthermore,

$$v_s^2 = \frac{ST}{4m_N} \left(1 + \left(3 + \frac{d \ln g_*}{d \ln T}\right)^{-1}\right), \quad (4)$$

$$\beta = \frac{1}{4} \left(1 + \left(3 + \frac{d \ln g_*}{d \ln T}\right)^{-1}\right). \quad (5)$$

The quantity \dot{q} is the specific energy deposition rate, which has four main contributions: heating due to ν_e and $\bar{\nu}_e$ absorption on nucleons ($\dot{q}_{\nu N}$), heating due to scattering of all neutrino flavors on electrons and positrons ($\dot{q}_{\nu e}$), cooling due to neutrino emission in e^+ or e^- absorption on nucleons (\dot{q}_{eN}), and cooling due to e^+e^- pair annihilation into neutrino-antineutrino pairs (\dot{q}_{e+e^-}). Numerically, these rates are [38, 49]:

$$\dot{q}_{\nu N} = 9.84 N_A \left[(1 - Y_e) L_{\nu_e, 51} \epsilon_{\nu_e, \text{MeV}}^2 + Y_e L_{\bar{\nu}_e, 51} \epsilon_{\bar{\nu}_e, \text{MeV}}^2 \right] \times \frac{1 - g_1(r)}{R_{\nu, 6}^2} \Phi(r)^6 \text{ MeV s}^{-1} \text{ g}^{-1}, \quad (6)$$

$$\dot{q}_{\nu e} = 2.17 N_A \frac{T_{\text{MeV}}^4}{\rho_8} \left(L_{\nu_e, 51} \epsilon_{\nu_e} + L_{\bar{\nu}_e, 51} \epsilon_{\bar{\nu}_e} + \frac{6}{7} L_{\nu_x, 51} \epsilon_{\nu_x} \right) \times \frac{1 - g_1(r)}{R_{\nu, 6}^2} \Phi(r)^5 \text{ MeV s}^{-1} \text{ g}^{-1}, \quad (7)$$

$$\dot{q}_{eN} = 2.27 N_A T_{\text{MeV}}^6 \text{ MeV s}^{-1} \text{ g}^{-1}, \quad (8)$$

$$\dot{q}_{e+e^-} = 0.144 N_A \frac{T_{\text{MeV}}^9}{\rho_8} \text{ MeV s}^{-1} \text{ g}^{-1}. \quad (9)$$

where N_A is the Avogadro number, $R_{\nu, 6}$ is the neutrinosphere radius in units of 10^6 cm, $L_{\nu, 51}$ is the neutrino luminosity in units of 10^{51} erg/s, $\epsilon = \sqrt{\langle E^3 \rangle / \langle E \rangle}$ and $\epsilon = \langle E^2 \rangle / \langle E \rangle$. The redshift factor $\Phi(r)$ is given by

$$\Phi(r) = \sqrt{\frac{1 - 2GM/R_\nu}{1 - 2GM/r}} \quad (10)$$

and the factor $(1 - g_1(r))$ represents the effect of the gravitational bending of the neutrino trajectories,

$$g_1(r) = \sqrt{1 - \left(\frac{R_\nu}{r}\right)^2 \left(\frac{1 - 2GM/r}{1 - 2GM/R_\nu}\right)}. \quad (11)$$

To completely specify the problem, one should supply (i) the luminosities and energy spectra of the electron neutrinos and antineutrinos, (ii) the properties of the protoneutron star—its mass and radius, and (iii) the appropriate physical boundary conditions at the starting and ending radii. The three boundary conditions we impose are the temperature and density at the PNS surface and, crucially, the pressure of the surrounding material, P_{far} . This surrounding pressure is considered fixed for a given snapshot, as discussed earlier, but is varied between the snapshots. It is dictated by the density of the surrounding material, ρ_s and its radiation entropy per baryon, S_s . The density, in turn, is controlled by the amount of matter plowed up by the expanding front shock, $M_{\text{plow}}(t)$ and the radius of the front shock, $R_s(t)$:

$$\rho_s(t) \sim M_{\text{plow}} / [(4\pi/3)R_s^3], \quad R_s = v_s t. \quad (12)$$

The value of $M_{\text{plow}}(t)$ depends on the progenitor density profile and the *mass cut* (the position of the mass element that separates ejected and accreted material). In our calculations, we take progenitor profiles from [50].

In order to convert $\rho_s(t)$ to $P_{\text{far}}(t)$, we impose pressure continuity across the boundary of the hot bubble. Let ρ_f be the far density of the outflow, S_f be the radiation entropy in it, and $S_s \sim 6$ be the radiation entropy of the surrounding material. The equality of the radiation pressures then implies that temperature is continuous, while the density jumps by the ratio of the radiation entropies: $\rho_s/\rho_f = S_f/S_s \sim 12$. This density jump at the edge of

the high-entropy hot bubble region is seen in 1D simulations and is commonly known as a contact discontinuity.

The system is solved numerically following the procedure developed in [36]. The boundary condition on the surrounding pressure is matched by “shooting” the initial velocity in the subsonic case and the position of the shock in the supersonic case. This procedure continuously covers the entire range of physical possibilities and self-consistently determines the nature of the outflow.

The second segment of the trajectory must be modeled for several seconds, during which neutron production takes place. During this time, the distribution of the lighter p -elements evolves (the peaks and troughs are smoothed by neutron capture), as well as the synthesis of ^{92}Nb takes place. The key physics observation is that the material behind the front shock is expanding approximately homologously, so that the velocities as a function of r follow the Hubble law. This is so because the entire region is in causal contact and the effects of gravity for $r > 10^3$ km on the density distribution are subdominant. The outflow material joins this expansion when the velocity computed in the first segment falls to the value predicted by the Hubble law. Typically, the transition happens at around $r \sim 10^3$ km, where the velocity is a fraction of that of the front shock. For example, when the front shock is at $R_s \sim 10^4$ and has $v_s \sim 10^4$ km/s, the transition velocity at 10^3 km is 10^3 km/s. The speed of the matter element remains a fixed fraction of the front shock speed, and its density is governed by Eq. (12). This physical model is in good agreement with the results in [43], as well as with the empirical parametrization of simulation results employed in [14].

The results of this procedure are shown in Fig. 3, where we show the nucleosynthesis calculations along different time snapshots. The heating rates, \dot{q}_i have been computed using an exponentially decreasing luminosity: $L_{\nu_\gamma}(t) = L_{\nu_\gamma}(t_0) e^{-(t-t_0)/\tau}$, with a time constant $\tau = 3$ s, as described below. Our model passes a number of qualitative and quantitative validation tests, when compared to the full 1D explosion simulations in the literature [43, 51]. At the basic level, heavier progenitor stars give rise to higher swept-up masses, resulting in higher surrounding pressures and subsonic outflows. In detail, our model reproduces intricate features of tran-

sient shocks, where termination shocks appear during a small time window, and then disappear, in good agreement with the $\sim 10 M_\odot$ progenitor simulations of [43].

B. Neutrino luminosities and spectra

Neutrinos streaming from the cooling PNS determine both the heating rate \dot{q} in the outflow equations and the neutron production rate for the nucleosynthesis network. In this work, we adopt a ‘‘pinched Fermi-Dirac’’ parametrization for the neutrino distributions [52]:

$$f_{\nu_\gamma} \propto \frac{1}{e^{E/T_{\nu_\gamma} - \eta_{\nu_\gamma}} + 1}, \quad (13)$$

where $\nu_\gamma \in \{\nu_e, \bar{\nu}_e\}$. The distribution for each species is specified with three parameters: the effective neutrino temperature T_{ν_γ} and the pinching parameter η_{ν_γ} —which together set the spectral shape—and the luminosity L_{ν_γ} , which fixes the flux normalization. These parameters are independent and not related by the black-body formula, reflecting the complex dynamics of neutrino decoupling.

We choose an exponentially decreasing luminosity, as described in Sec. II A. It is important to account for this decrease in luminosity within each nucleosynthesis snapshot calculation, in order to correctly estimate the number of neutron captures during the third stage in Fig. 2 ($T < 1.5$ GK). An overestimation of late-time neutron captures could potentially turn material that is proton-rich at 1.5 GK into a neutron-rich state afterward [19]. This effect would be expected to be stronger in subsonic outflows because of the greater relative proximity to the PNS, or at high entropies because of the relative underabundance of seeds relative to the number of late-time neutrons (e.g., the $S = 140$ case in Ref. [31]).

Most of the yields are generated in the first 1–2 s after shock launch, in the HYTEW (see Sec. II D for details). The spectral parameters T_{ν_γ} and η_{ν_γ} are generally found in simulations not to vary significantly in this window (e.g., [53]). Therefore, for simplicity, we hold these parameters, and the protoneutron star radius R_{PNS} , fixed throughout our calculation. The final outcome is thus not particularly sensitive to variations of these physical parameters beyond ~ 2 s post-shock.

The neutrino and PNS parameters used in our calculations are presented in Table I. The ratios of the neutrino and antineutrino luminosities ensure $Y_e \simeq 0.6$ in the outflow, leading to an optimal νp -process (cf. [14]). For the $9.5 M_\odot$ model, we use luminosities that are 30% higher than for the heavy progenitor calculations, as well as a smaller pinching parameter for $\bar{\nu}_e$. These choices enabled us to obtain a supersonic outflow solution with a wind-termination shock that qualitatively resembled the parametrized profiles in [31], facilitating comparison of results. Neutrino spectra are known to vary sensitively between simulations, and can be further impacted by other physics such as flavor oscillations. While the values chosen here (and in other literature, e.g., [14, 31])

are physically plausible, a follow-up investigation of the impact of different spectra is highly motivated.

Parameter	Value	
	13 M_\odot simulation	9.5 M_\odot simulation
L_{ν_e} (1 s)	7×10^{51} erg/s	9.1×10^{51} erg/s
$L_{\bar{\nu}_e}$ (1 s)	5.74×10^{51} erg/s	7.46×10^{51} erg/s
$\langle E_{\nu_e} \rangle$	9.7 MeV	9.7 MeV
$\langle E_{\bar{\nu}_e} \rangle$	11.7 MeV	11.7 MeV
η_{ν_e}	2.1	2.1
$\eta_{\bar{\nu}_e}$	1.5	0.7
M_{PNS}	1.8 M_\odot	1.4 M_\odot
R_{PNS}	19 km	19 km
$Y_{e,0}$	0.6	0.6

TABLE I. Neutrino and protoneutron star parameters used in the 13 M_\odot and 9.5 M_\odot simulations presented in Sec. I. The luminosities at time t were taken to be $L_{\nu_\gamma}(t) = L_{\nu_\gamma}(t_0)e^{-(t-t_0)/\tau}$, with $\tau = 3$ s, whereas the average energies $\langle E_{\nu_\gamma} \rangle$ and pinching parameters η_{ν_γ} were held fixed.

Note that the neutrino spectral parameters values specified in Table I are from the point of view of a distant observer. In the outflow and nucleosynthesis calculations, the neutrino fluxes and energies in the vicinity of the PNS are calculated relative to their values at infinity using the appropriate gravitational blue-shift factors (powers of $(1 - 2GM/r)^{-1/2}$). The geometric dilution of the neutrino fluxes is assumed in accordance with an isotropic emission (in outward directions) from a spherical surface with radius R_ν , and is given by

$$\mathcal{D}(r) = \frac{1}{2} \left(1 - \sqrt{1 - \frac{R_\nu^2}{r^2}} \right). \quad (14)$$

In the outflow calculations, we take $R_\nu = R_{\text{PNS}}$.

C. Nucleosynthesis calculations with SkyNet

The nucleosynthesis network calculations were carried out using SkyNet [54, 55], an open source reaction network, which adopts the majority of nuclear reaction rates from the ReaLib library, version 2.2 [56, 57]. Starting with the special_reaction_library_rebased branch of SkyNet, two principal modifications were made: (i) the triple- α reaction rate was boosted by in-medium enhancement effects [31, 33]; and (ii) a crucial bug in ReaLib describing the decay of ^{92}Nb was corrected.

The modified triple- α rate was implemented using the publicly available code [58] from the authors of Ref. [31], with a number of further modifications, including the general-relativistic (GR) corrections and time-dependent neutrino luminosities, both as described above. The GR corrections are found to increase the entropy per baryon

by about $\Delta S \sim 5$, which decreases seed production during stage I, as desired.

The `ReacLib` issue is easy to state: any ^{92}Nb made in `SkyNet` undergoes a β -decay $^{92}\text{Nb} \rightarrow ^{92}\text{Mo}$ on a timescale of $\mathcal{O}(100\text{ s})$. This behavior is incorrect: this decay channel is strongly forbidden and is neither observed nor expected [59]. The bug drives any ^{92}Nb produced back to ^{92}Mo , thus unfortunately reinforcing the shielding argument. Instead, ^{92}Nb was measured to decay to ^{92}Zr by electron capture with a half-life of $\sim 35\text{ Myr}$ [60–62]. The long-lived property makes ^{92}Nb a promising cosmochronometer [34, 35], although the astrophysical conclusions drawn from these analyses should be reevaluated in view of the findings in the present paper.

The issue is traced to the rate fitting coefficient a_0 ; changing it from $-4.260150\text{e}+00$ to $-4.260150\text{e}+01$ puts the decay half-life at its lower limit $\sim 10^{11}\text{ yr}$ [63]. We implement this correction, which is physically equivalent to setting the rate to zero. Additional fix in `SkyNet` involved modifying the normalization of the neutrino spectrum. This was necessary to reproduce the correct luminosities for the “pinched” spectra used here.

In the results shown here, we used the density profiles from the outflow calculation as an input to `SkyNet` and permitted it to calculate the temperature using its internal self-heating subroutine. As a consistency check, we also ran calculations where both the *density and temperature* profiles were provided as inputs to `SkyNet`.

Each nucleosynthesis run commences at a temperature of 10 GK ($\simeq 0.86\text{ MeV}$), in conditions of nuclear statistical equilibrium (NSE). `SkyNet` tracks the nuclear abundance $Y_{A,Z}$ of each species using an NSE calculation until a temperature of 9 GK is reached, following which it switches to a full network calculation. Figure 5 depicts the radial evolution of certain selected abundances, plotted as a function of the outflow temperature, for a particular snapshot of the $13 M_{\odot}$ progenitor model.

D. Computing integrated yields

In order to obtain the integrated nuclide yields, we calculate the nucleosynthetic output along a sequence of snapshots of the neutrino-driven outflow, corresponding to different times after shock launch. The yields obtained for each snapshot are then multiplied by the corresponding mass outflow rates and added up. The results can then be compared with the observed nuclide abundances in the solar system [11]. For a nuclide (A, Z) , we define the time-averaged abundance $\langle Y_{A,Z} \rangle$ as:

$$\langle Y_{A,Z} \rangle = \frac{\int Y_{A,Z}(t_{\text{ps}}) \dot{M}(t_{\text{ps}}) dt_{\text{ps}}}{\int \dot{M}(t_{\text{ps}}) dt_{\text{ps}}}, \quad (15)$$

where $Y_{A,Z}(t_{\text{ps}})$ is the abundance at a post-shock time t_{ps} , and $\dot{M}(t_{\text{ps}})$ is the corresponding mass outflow rate which is obtained from solving the outflow equations from Sec. II A. The time-averaged mass fraction of the nuclide

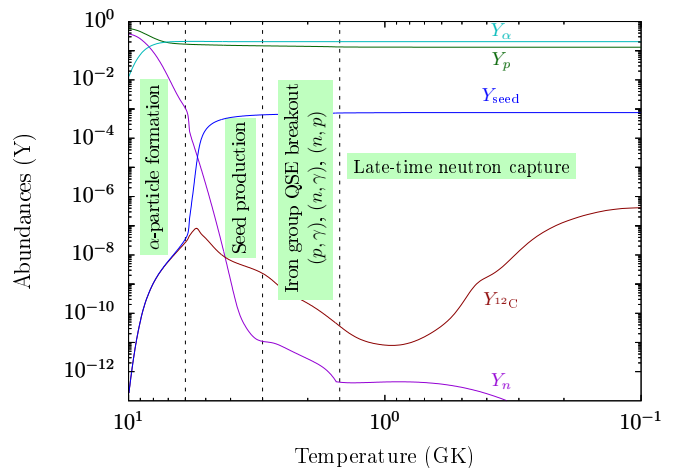


FIG. 5. Radial evolution of the following nuclear abundances as a function of outflow temperature: n , p , ^4He , ^{12}C , and ‘seed’ nuclei ($A \geq 12$), with temperature for a 1.4 s post-shock outflow profile snapshot of the $13 M_{\odot}$ progenitor model.

(A, Z) can then be obtained as $\langle X_{A,Z} \rangle = A \langle Y_{A,Z} \rangle$, provided the abundances are normalized so that the sum $\sum A Y_{A,Z}$ over all nuclides adds up to 1.

The isotopic *production factor* [14] is $f_{A,Z} = \langle X_{A,Z} \rangle / X_{A,Z}^{\odot}$, where $X_{A,Z}^{\odot}$ is the mass fraction of that isotope in the solar system. We take the solar system mass fractions of different isotopes from [11], where detailed isotopic abundances are tabulated from meteoritic studies of Carbonaceous Chondrites. In Ref. [11], all the measured solar system abundances $Y_{A,Z}$ are normalized so that silicon has a total abundance of 10^6 . While converting these into mass fractions, one must use the appropriate normalization factor, which may be obtained by comparing the abundance of hydrogen (2.431×10^{10}) to its observed mass fraction (0.7110). Analysis of meteoritic compositions, in combination with galactic chemical evolution models, have shown that the ratio of $^{92}\text{Nb}/^{92}\text{Mo}$ at production has to be in the range 10^{-3} – 10^{-2} [5, 34, 40, 41]. Hence, we present the “production factor” for ^{92}Nb normalized to 3×10^{-3} times the meteoritic ^{92}Mo abundance.

The production factors are a means of comparing the *relative abundances* of different isotopes synthesized in an environment. Isotopes with $f_{A,Z}$ not less than a tenth of the largest production factor f_{max} can be considered to be co-produced in significant quantities [14, 30]. The production factors of various p -nuclides of interest, for the $13 M_{\odot}$ and $9.5 M_{\odot}$ progenitor calculations, are depicted in the bottom panels of Fig. 3. Fig. 6 shows the corresponding results for an $18 M_{\odot}$ progenitor model. A qualitative agreement is observed between the 13 and $18 M_{\odot}$ models, demonstrating that the νp -mechanism works under subsonic outflow conditions for a broad range of progenitor masses.

Another metric often used for evaluating the efficacy of a nucleosynthetic process is the *overproduction fac-*

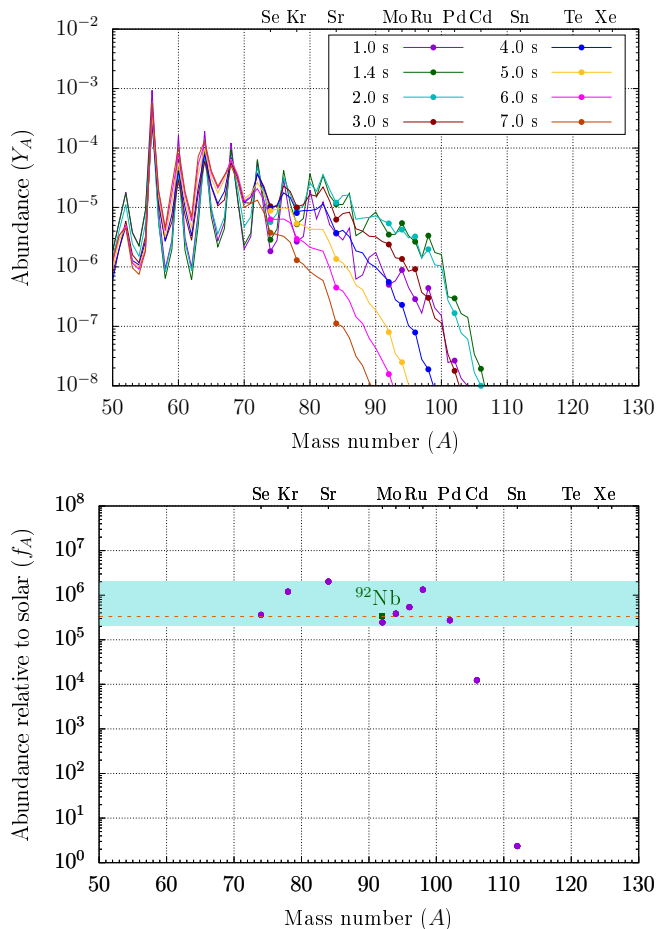


FIG. 6. *Top*: Time snapshots of nucleosynthetic yields for an $18 M_{\odot}$ progenitor model. *Bottom*: Integrated production factors (abundances relative to solar) of the p -nuclides of interest. The snapshot-by-snapshot yields as well as the integrated yields are qualitatively similar to those of the $13 M_{\odot}$ progenitor calculation (Fig. 3 left panels). Note that the high yield time window is reached at a *slightly* later time for the $18 M_{\odot}$ model (1.4–2 s post-shock) as compared to the $13 M_{\odot}$ model (1.0–1.6 s), but still early enough for the mass-outflow rates, and hence the integrated yields to remain sizeable.

tor [14, 32]. It is defined as $f_{A,Z} \times (M_{\text{out}}/M_{\text{ejec}})$, i.e., the product of $f_{A,Z}$ and an astrophysical dilution factor which is the ratio of the total mass driven out in the neutrino-driven outflow (M_{out}) and the total mass ejected in the explosion (M_{ejec}). The outflow mass $M_{\text{out}} = \int \dot{M}(t_{\text{ps}}) dt_{\text{ps}}$ is obtained from the solutions of the outflow equations and the total ejecta mass is $M_{\text{ejec}} \approx M_{\text{prog}} - M_{\text{PNS}}$, where M_{prog} is the progenitor mass. The overproduction factor is used for comparing the *absolute* abundances of isotopes. To explain the solar system abundance of an isotope, its overproduction factor in a supernova event must be $\gtrsim 10$ [14, 32].

One typically finds $M_{\text{out}} \sim 10^{-3} M_{\odot}$ and $M_{\text{ejec}} \sim 10 M_{\odot}$ in a core-collapse supernova environment. For both the 13 and $18 M_{\odot}$ models, we find the total outflow

mass to be $M_{\text{out}} \approx 4.4\text{--}4.5 \times 10^{-4} M_{\odot}$. As seen in Figs. 3 and 6, for both these progenitors, $f_{A,Z}(M_{\text{out}}/M_{\text{ejec}}) \gtrsim 10$ is satisfied for p -nuclides up to ^{102}Pd . The values of the production factor $f_{A,Z}$ which correspond to an overproduction factor of 10 in each case are shown using a red dashed line. In contrast, the integrated yields for the $A > 90$ nuclei in the $9.5 M_{\odot}$ model (bottom right panel of Fig. 3) can clearly be seen to be deficient, both in an absolute sense and in comparison to the lighter p -nuclides.

E. Dependence on the PNS radius

The amount of seed production is controlled by the efficiency of the triple- α reaction, which depends on the matter density at temperatures of $\sim 3\text{--}6$ GK. This, in turn, is controlled by the value of entropy per baryon in the outflow, S . The dependence of S on the physical parameters—neutrino luminosity (L_{ν}), average energy ($\langle E_{\nu} \rangle$), PNS mass (M_{PNS}) and radius (R_{PNS})—is approximately $S \propto L_{\nu}^{-1/6} \langle E_{\nu} \rangle^{-1/3} R_{\text{PNS}}^{-2/3} M_{\text{PNS}}$ [38]. This scaling law shows that S is mainly determined by the PNS mass and radius. Physically, the more massive and compact the PNS, the deeper the gravitational potential well, and the outflow is thus required to have more radiation energy per baryon, $T^4/n \propto TS$, to become unbound.

Most of the yields are produced in the HYTW, which occurs at $\mathcal{O}(1\text{--}2\text{ s})$ after the shock revival. At such times, self-consistent 3D simulations almost universally find $R_{\text{PNS}} \sim 17\text{--}22$ km [45–47]. We have seen that using $R_{\text{PNS}} \sim 19$ km implies that $M_{\text{PNS}} \gtrsim 1.7 M_{\odot}$. These results are supported by modern simulations which find for massive progenitors (which have subsonic outflows) extended accretion and hence M_{PNS} above the Chandrasekhar value [45–47]. They are also supported by the measurements of pulsars in binary- and multiple-star systems that the upper limit on the neutron star mass is at least $\sim 2 M_{\odot}$ [64–66]. Nearly 20% of the measured NS masses are $1.8 M_{\odot}$ or greater, and it has been suggested that the mass distribution is bimodal, with a secondary peak centered at $M_{\text{NS}} \sim 1.8 M_{\odot}$ [66]. Notice that the masses of cold neutron stars are 5–10% lower than during the HYTW when a significant amount of energy and lepton number still remains in the PNS.

To complete this argument, in Fig. 7 we report the variation of νp -process yields with PNS radius, with the PNS mass kept fixed at $1.8 M_{\odot}$. Compact objects with $R_{\text{PNS}} \sim 14$ km can produce p -nuclides even up to $A \sim 120\text{--}130$, while for larger radii $R_{\text{PNS}} > 20$ km, the yields are negligible beyond ^{84}Sr . The observed solar abundances are well reproduced by $R \sim 18\text{--}20$ km.

ACKNOWLEDGMENTS

The majority of this work was carried out at SLAC, where it was supported by the U.S. Department of Energy under contract number DE-AC02-76SF00515. We

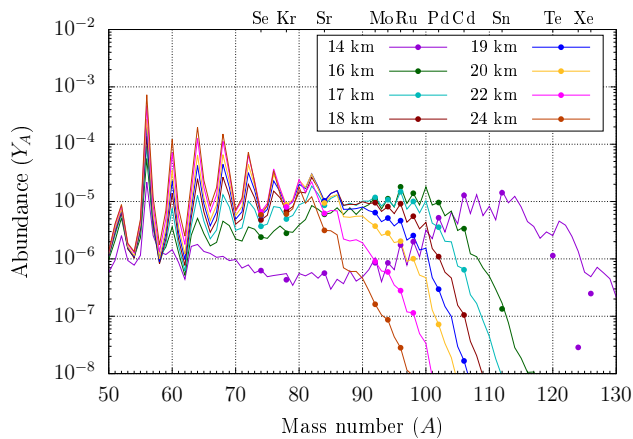


FIG. 7. νp -process yields for different proton-neutron star radii ranging from 14–24 km. The mass of the proton-neutron star is kept fixed at $1.8 M_{\odot}$. Clearly, more compact objects are better suited for more efficient νp -process.

also thank the Kavli Institute for Theoretical Physics

(KITP), the Institute for Nuclear Theory (INT) at the University of Washington, and the Mainz Institute for Theoretical Physics (MITP), where parts of this work were completed and preliminary results presented. This research was supported at KITP by the National Science Foundation under Grants No. NSF PHY-1748958 and PHY-2309135, at INT by the U.S. Department of Energy grant No. DE-FG02-00ER41132, and at MITP by the Cluster of Excellence PRISMA+ (Project ID 39083149). AVP also acknowledges support from the U.S. Department of Energy under contract number DE-FG02-87ER40328 at the University of Minnesota, as well as partial travel support from the Network for Neutrinos, Nuclear Astrophysics, and Symmetries (N3AS), funded by the National Science Foundation under grant no. PHY-2020275. The work of PM is supported in part by the Neutrino Theory Network Program Grant under award number DE-AC02-07CHI11359. We gladly acknowledge C. Horowitz, G. McLaughlin, S. Reddy, R. Surman, and G. Martinez-Pinedo for useful discussions and I. Padilla-Gay for helpful feedback on the manuscript.

-
- [1] M. E. Burbidge, G. R. Burbidge, W. A. Fowler, and F. Hoyle, Synthesis of the elements in stars, *Rev. Mod. Phys.* **29**, 547 (1957).
- [2] F. Kaeppeler, R. Gallino, S. Bisterzo, and W. Aoki, The s Process: Nuclear Physics, Stellar Models, Observations, *Rev. Mod. Phys.* **83**, 157 (2011), [arXiv:1012.5218 \[astro-ph.SR\]](#).
- [3] M. Arnould, S. Goriely, and K. Takahashi, The r-process of stellar nucleosynthesis: Astrophysics and nuclear physics achievements and mysteries, *Phys. Rept.* **450**, 97 (2007), [arXiv:0705.4512 \[astro-ph\]](#).
- [4] A. G. W. Cameron, Nuclear astrophysics, *Ann. Rev. Nucl. Part. Sci.* **8**, 299 (1958).
- [5] T. Rauscher, N. Dauphas, I. Dillmann, C. Fröhlich, Z. Fülöp, and G. Gyürky, Constraining the astrophysical origin of the p-nuclei through nuclear physics and meteoritic data, *Reports on Progress in Physics* **76**, 066201 (2013), [arXiv:1303.2666 \[astro-ph.SR\]](#).
- [6] S. E. Woosley and W. M. Howard, The p-processes in supernovae., *Astrophys. J. Suppl.* **36**, 285 (1978).
- [7] W. M. Howard, B. S. Meyer, and S. E. Woosley, A New Site for the Astrophysical Gamma-Process, *Astrophys. J. Letters* **373**, L5 (1991).
- [8] C. Travaglio, F. K. Röpke, R. Gallino, and W. Hillebrandt, Type ia supernovae as sites of the p-process: Two-dimensional models coupled to nucleosynthesis, *The Astrophysical Journal* **739**, 93 (2011), [astro-ph/1106.0582](#).
- [9] M. Arnould and S. Goriely, The p-process of stellar nucleosynthesis: astrophysics and nuclear physics status, *Phys. Rept.* **384**, 1 (2003).
- [10] S. Wanajo, The rp-process in neutrino-driven winds, *Astrophys. J.* **647**, 1323 (2006), [arXiv:astro-ph/0602488](#).
- [11] K. Lodders, Solar System Abundances and Condensation Temperatures of the Elements, *ApJ* **591**, 1220 (2003).
- [12] C. Travaglio, R. Gallino, T. Rauscher, F. K. Röpke, and W. Hillebrandt, Testing the role of sne ia for galactic chemical evolution of p-nuclei with two-dimensional models and with s-process seeds at different metallicities, *The Astrophysical Journal* **799**, 54 (2015), [astro-ph/1411.2399](#).
- [13] T. Rauscher, Challenges in nucleosynthesis of trans-iron elements, *AIP Adv.* **4**, 041012 (2014), [arXiv:1403.2015 \[astro-ph.SR\]](#).
- [14] S. Wanajo, H.-T. Janka, and S. Kubono, Uncertainties in the nu p-process: supernova dynamics versus nuclear physics, *Astrophys. J.* **729**, 46 (2011), [arXiv:1004.4487 \[astro-ph.SR\]](#).
- [15] D. D. Clayton, *Principles of stellar evolution and nucleosynthesis.* (1984).
- [16] H. Schatz *et al.*, rp-process nucleosynthesis at extreme temperature and density conditions, *Phys. Rept.* **294**, 167 (1998).
- [17] C. Fröhlich, G. Martinez-Pinedo, M. Liebendorfer, F. K. Thielemann, E. Bravo, W. R. Hix, K. Langanke, and N. T. Zinner, Neutrino-induced nucleosynthesis of $A > 64$ nuclei: the nu p-process, *Phys. Rev. Lett.* **96**, 142502 (2006), [arXiv:astro-ph/0511376](#).
- [18] J. Pruet, R. D. Hoffman, S. E. Woosley, H. T. Janka, and R. Buras, Nucleosynthesis in early supernova winds. 2. the role of neutrinos, *Astrophys. J.* **644**, 1028 (2006), [arXiv:astro-ph/0511194 \[astro-ph\]](#).
- [19] A. Arcones, C. Fröhlich, and G. Martinez-Pinedo, Impact of supernova dynamics on the νp -process, *Astrophys. J.* **750**, 18 (2012), [arXiv:1112.4651 \[astro-ph.SR\]](#).
- [20] M. Eichler, K. Nakamura, T. Takiwaki, T. Kuroda, K. Kotake, M. Hempel, R. Cabezón, M. Liebendorfer, and F.-K. Thielemann, Nucleosynthesis in 2D Core-Collapse Supernovae of 11.2 and 17.0 M_{\odot} Progenitors: Implications for Mo and Ru Production, *J. Phys. G* **45**, 014001 (2018), [arXiv:1708.08393 \[astro-ph.SR\]](#).

- [21] N. Nishimura, T. Rauscher, R. Hirschi, G. Cescutti, A. S. J. Murphy, and C. Fröhlich, Uncertainties in νp -process nucleosynthesis from Monte Carlo variation of reaction rates, *Mon. Not. Roy. Astron. Soc.* **489**, 1379 (2019), [arXiv:1907.13129 \[astro-ph.SR\]](#).
- [22] T. Rauscher, N. Nishimura, G. Cescutti, R. Hirschi, A. S. J. Murphy, and C. Fröhlich, Impact of Uncertainties in Astrophysical Reaction Rates on Nucleosynthesis in the νp Process, *JPS Conf. Proc.* **31**, 011026 (2020), [arXiv:1909.03235 \[astro-ph.HE\]](#).
- [23] S. Fujibayashi, T. Yoshida, and Y. Sekiguchi, Nucleosynthesis in neutrino-driven winds in hypernovae, *Astrophys. J.* **810**, 115 (2015), [arXiv:1507.05945 \[astro-ph.HE\]](#).
- [24] H. Sasaki, T. Kajino, T. Takiwaki, T. Hayakawa, A. B. Balantekin, and Y. Pehlivan, Possible effects of collective neutrino oscillations in three-flavor multiangle simulations of supernova νp processes, *Phys. Rev. D* **96**, 043013 (2017), [arXiv:1707.09111 \[astro-ph.HE\]](#).
- [25] Z. Xiong, A. Sieverding, M. Sen, and Y.-Z. Qian, Potential Impact of Fast Flavor Oscillations on Neutrino-driven Winds and Their Nucleosynthesis, *Astrophys. J.* **900**, 144 (2020), [arXiv:2006.11414 \[astro-ph.HE\]](#).
- [26] H. Sasaki, Y. Yamazaki, T. Kajino, M. Kusakabe, T. Hayakawa, M.-K. Cheoun, H. Ko, and G. J. Mathews, Impact of Hypernova νp -process Nucleosynthesis on the Galactic Chemical Evolution of Mo and Ru, *Astrophys. J.* **924**, 29 (2022), [arXiv:2106.01679 \[astro-ph.GA\]](#).
- [27] H. Sasaki, Y. Yamazaki, T. Kajino, and G. J. Mathews, Effects of Hoyle state de-excitation on νp -process nucleosynthesis and Galactic chemical evolution, (2023), [arXiv:2307.02785 \[astro-ph.HE\]](#).
- [28] J. L. Fisker, R. D. Hoffman, and J. Pruet, On the Origin of the Lightest Molybdenum Isotopes, *Astrophys. J. Lett.* **690**, L135 (2009), [arXiv:0711.1502 \[astro-ph\]](#).
- [29] J. Bliss and A. Arcones, Nucleosynthesis of Mo in neutrino-driven winds, *PoS NICKIII*, 073 (2015).
- [30] J. Bliss, A. Arcones, and Y.-Z. Qian, Production of Mo and Ru isotopes in neutrino-driven winds: implications for solar abundances and presolar grains, *Astrophys. J.* **866**, 105 (2018), [arXiv:1804.03947 \[astro-ph.HE\]](#).
- [31] S. Jin, L. F. Roberts, S. M. Austin, and H. Schatz, Enhanced triple- α reaction reduces proton-rich nucleosynthesis in supernovae, *Nature* **588**, 57 (2020).
- [32] S. E. Woosley, J. R. Wilson, G. J. Mathews, R. D. Hoffman, and B. S. Meyer, The r process and neutrino heated supernova ejecta, *Astrophys. J.* **433**, 229 (1994).
- [33] M. Beard, S. M. Austin, and R. Cyburt, Enhancement of the Triple Alpha Rate in a Hot Dense Medium, *Phys. Rev. Lett.* **119**, 112701 (2017), [arXiv:1708.07204 \[nucl-th\]](#).
- [34] M. Lugaro, M. Pignatari, U. Ott, K. Zuber, C. Travaglio, G. Gyurky, and Z. Fulop, Origin of the p-process radionuclides ^{92}Nb and ^{146}Sm in the early Solar System and inferences on the birth of the Sun, *Proc. Nat. Acad. Sci.* **113**, 907 (2016), [arXiv:1601.05986 \[astro-ph.SR\]](#).
- [35] M. K. Haba, Y.-J. Lai, J.-F. Wotzlaw, A. Yamaguchi, M. Lugaro, and M. Schönbachler, Precise initial abundance of Niobium-92 in the Solar System and implications for p-process nucleosynthesis, *Proc. Nat. Acad. Sci.* **118**, 2017750118 (2021).
- [36] A. Friedland and P. Mukhopadhyay, Near-critical supernova outflows and their neutrino signatures, *Phys. Lett. B* **834**, 137403 (2022), [arXiv:2009.10059 \[astro-ph.HE\]](#).
- [37] R. C. Duncan, S. L. Shapiro, and I. Wasserman, Neutrino-driven winds from young, hot neutron stars, *Astrophys. J.* **309**, 141 (1986).
- [38] Y. Z. Qian and S. E. Woosley, Nucleosynthesis in neutrino driven winds: 1. The Physical conditions, *Astrophys. J.* **471**, 331 (1996), [arXiv:astro-ph/9611094](#).
- [39] T. A. Thompson, A. Burrows, and B. S. Meyer, The Physics of proton-neutron star winds: implications for r-process nucleosynthesis, *Astrophys. J.* **562**, 887 (2001), [arXiv:astro-ph/0105004 \[astro-ph\]](#).
- [40] T. Iizuka, Y.-J. Lai, W. Akram, Y. Amelin, and M. Schönbachler, The initial abundance and distribution of ^{92}Nb in the Solar System, *Earth and Planetary Science Letters* **439**, 172 (2016), [arXiv:1602.00966 \[astro-ph.SR\]](#).
- [41] Y. Hibiya, T. Iizuka, H. Enomoto, and T. Hayakawa, Evidence for Enrichment of Niobium-92 in the Outer Protosolar Disk, *Astrophys. J. Lett.* **942**, L15 (2023).
- [42] N. Dauphas, T. Rauscher, B. Marty, and L. Reisberg, Short-lived p-nuclides in the early solar system and implications on the nucleosynthetic role of x-ray binaries, *Nuclear Physics A* **719**, C287 (2003).
- [43] T. Fischer, S. C. Whitehouse, A. Mezzacappa, F. K. Thielemann, and M. Liebendorfer, Proton-neutron star evolution and the neutrino driven wind in general relativistic neutrino radiation hydrodynamics simulations, *Astron. Astrophys.* **517**, A80 (2010), [arXiv:0908.1871 \[astro-ph.HE\]](#).
- [44] L. F. Roberts and S. Reddy, Neutrino Signatures From Young Neutron Stars, [arXiv:1612.03860 \[astro-ph.HE\]](#) (2016).
- [45] A. Burrows, D. Radice, and D. Vartanyan, Three-dimensional supernova explosion simulations of 9-, 10-, 11-, 12-, and 13- M_{\odot} stars, *Mon. Not. Roy. Astron. Soc.* **485**, 3153 (2019), [arXiv:1902.00547 \[astro-ph.SR\]](#).
- [46] R. Bollig, N. Yadav, D. Kresse, H. T. Janka, B. Müller, and A. Heger, Self-consistent 3D Supernova Models From -7 Minutes to $+7$ s: A 1-bethe Explosion of a $\sim 19 M_{\odot}$ Progenitor, *Astrophys. J.* **915**, 28 (2021), [arXiv:2010.10506 \[astro-ph.HE\]](#).
- [47] D. Vartanyan, A. Burrows, D. Radice, A. M. Skinner, and J. Dolence, A Successful 3D Core-Collapse Supernova Explosion Model, *Mon. Not. Roy. Astron. Soc.* **482**, 351 (2019), [arXiv:1809.05106 \[astro-ph.HE\]](#).
- [48] A. Burrows and D. Vartanyan, Core-Collapse Supernova Explosion Theory, *Nature* **589**, 29 (2021), [arXiv:2009.14157 \[astro-ph.SR\]](#).
- [49] C. Y. Cardall and G. M. Fuller, General relativistic effects in the neutrino driven wind and r process nucleosynthesis, *Astrophys. J. Lett.* **486**, L111 (1997), [arXiv:astro-ph/9701178](#).
- [50] T. Sukhbold, T. Ertl, S. E. Woosley, J. M. Brown, and H. T. Janka, Core-Collapse Supernovae from 9 to 120 Solar Masses Based on Neutrino-powered Explosions, *Astrophys. J.* **821**, 38 (2016), [arXiv:1510.04643 \[astro-ph.HE\]](#).
- [51] A. Arcones, H.-T. Janka, and L. Scheck, Nucleosynthesis-relevant conditions in neutrino-driven supernova outflows. 1. Spherically symmetric hydrodynamic simulations, *Astron. Astrophys.* **467**, 1227 (2007), [arXiv:astro-ph/0612582 \[astro-ph\]](#).
- [52] M. T. Keil, G. G. Raffelt, and H.-T. Janka, Monte Carlo study of supernova neutrino spectra formation, *Astrophys. J.* **590**, 971 (2003), [arXiv:astro-ph/0208035 \[astro-ph\]](#).
- [53] L. Hudepohl, B. Müller, H. T. Janka, A. Marek, and

- G. G. Raffelt, Neutrino Signal of Electron-Capture Supernovae from Core Collapse to Cooling, *Phys. Rev. Lett.* **104**, 251101 (2010), [Erratum: *Phys. Rev. Lett.* 105,249901(2010)], [arXiv:0912.0260](https://arxiv.org/abs/0912.0260) [astro-ph.SR].
- [54] J. Lippuner and L. F. Roberts, SkyNet: A modular nuclear reaction network library, *Astrophys. J. Suppl.* **233**, 18 (2017), [arXiv:1706.06198](https://arxiv.org/abs/1706.06198) [astro-ph.HE].
- [55] ‘SkyNet’ source code available at: <https://bitbucket.org/jlippuner/skynet/src/master/>.
- [56] R. H. Cyburt, A. M. Amthor, R. Ferguson, Z. Meisel, K. Smith, S. Warren, A. Heger, R. D. Hoffman, T. Rauscher, A. Sakharuk, H. Schatz, F. K. Thielemann, and M. Wiescher, The JINA REACLIB Database: Its Recent Updates and Impact on Type-I X-ray Bursts, *Astrophys. J. Supplement Series* **189**, 240 (2010).
- [57] JINA Reaclib Database, available at: <https://reaclib.jinaweb.org/>.
- [58] ‘TripleAlphaInMediumEnhancement’ source code available at: <https://bitbucket.org/lroberts/triplealphainmediumenthancement/src/master/>.
- [59] C. M. Baglin, Nuclear Data Sheets for $A = 92$, *Nucl. Data Sheets* **113**, 2187 (2012).
- [60] T. Makino and M. Honda, Half-life of ^{92}Nb , *Geochimica et Cosmochimica Acta* **41**, 1521 (1977).
- [61] D. R. Nethaway, A. L. Prindle, and R. A. Van Konynenburg, Half-life of ^{92}Nb , *Phys. Rev. C* **17**, 1409 (1978).
- [62] S. Heinitz, I. Kajan, and D. Schumann, How accurate are half-life data of long-lived radionuclides?, *Radiochimica Acta* **110**, 589 (2022).
- [63] J. K. Tuli, Nuclear Wallet Cards, 8th Edition, National Nuclear Data Center, Brookhaven National Laboratory, New York, https://www.nndc.bnl.gov/nudat3/indx_sigma.jsp (2011).
- [64] F. Özel, D. Psaltis, R. Narayan, and A. Santos Villareal, On the Mass Distribution and Birth Masses of Neutron Stars, *Astrophys. J.* **757**, 55 (2012), [arXiv:1201.1006](https://arxiv.org/abs/1201.1006) [astro-ph.HE].
- [65] F. Özel and P. Freire, Masses, Radii, and the Equation of State of Neutron Stars, *Ann. Rev. Astron. Astrophys.* **54**, 401 (2016), [arXiv:1603.02698](https://arxiv.org/abs/1603.02698) [astro-ph.HE].
- [66] J. Antoniadis, T. M. Tauris, F. Özel, E. Barr, D. J. Champion, and P. C. C. Freire, The millisecond pulsar mass distribution: Evidence for bimodality and constraints on the maximum neutron star mass, (2016), [arXiv:1605.01665](https://arxiv.org/abs/1605.01665) [astro-ph.HE].